Optics Letters

Telecom InP/InGaAs nanolaser array directly grown on (001) silicon-on-insulator

YU HAN,[1] WAI KIT NG,[2] YING XUE,[1] QIANG LI,[1] KAM SING WONG,[2] AND KEI MAY LAU[1,*] (iD)

[1]Department of Electronic and Computer Engineering, Hong Kong University of Science and Technology, Clear Water Bay, Kowloon, Hong Kong, China
[2]Department of Physics and William Mong Institute of Nano Science and Technology, Hong Kong University of Science and Technology, Clear Water Bay, Kowloon, Hong Kong, China
*Corresponding author: eekmlau@ust.hk

A compact, efficient, and monolithically grown III–V laser source provides an attractive alternative to bonding off-chip lasers for Si photonics research. Although recent demonstrations of microlasers on (001) Si wafers using thick metamorphic buffers are encouraging, scaling down the laser footprint to nanoscale and operating the nanolasers at telecom wavelengths remain significant challenges. Here, we report a monolithically integrated in-plane InP/InGaAs nanolaser array on (001) silicon-on-insulator (SOI) platforms with emission wavelengths covering the entire C band (1.55 μm). Multiple InGaAs quantum wells are embedded in high-quality InP nanoridges by selective-area growth on patterned (001) SOI. Combined with air-cladded InP/Si optical cavities, room-temperature operation at multiple telecom bands is obtained by defining different cavity lengths with lithography. The demonstration of telecom-wavelength monolithic nanolasers on (001) SOI platforms presents an important step towards fully integrated Si photonics circuits. © 2019 Optical Society of America

Recent advances in Si-based optoelectronic integrated circuits (OEICs) have been underpinned by the development of some key components such as low-loss waveguides, high-speed optical modulators, and sensitive photodetectors [1]. However, the final brick, an efficient and scalable on-chip III–V light source, is still missing [2,3]. To bridge the gap between cost-effective electronics and power-efficient photonics, direct heteroepitaxy of III–V coherent laser sources on a Si substrate offers potential lower cost and wider scalability as compared to chip scale bonding approaches [4]. Through buffer engineering, highly efficient electrical injection III–V quantum dot lasers with promising performance have recently been demonstrated [5–7]. Yet scaling device footprint to nanometer scale is highly sought-after for ultralow energy consumption and dense integration of Si-based OEICs [8–10]. Prevailing approaches using vertically aligned III–V nanowires, with a helical GaAs/InGaAs

nanopillar cavity [11], GaAs/AlGaAs Fabry–Perot (FP) cavity [12], and InGaAs/InGaP photonic crystal nanobeam cavity [13], have successfully integrated nanolasers on (111) Si substrates, which, however, are not easily made compatible with present Si photonics chips fabricated on the (001) Si platform. In addition, the operation wavelength is restricted to below the E band (<1460 nm), possibly due to the degrading mode confinement and the exacerbating optical loss at longer wavelengths [14,15]. Recently, well-aligned in-plane III–V distributed-feedback nanolasers have been incorporated into the complementary metal-oxide semiconductor (CMOS) lines using III–V nanoridges selectively grown on patterned 300 mm (001) Si wafers [16,17]. However, the nanolasers were grown on bulk Si substrates, and on-chip mode confinement was realized by either suspending the nanoridges in air or growing large nanoridge structures from narrow trenches [18]. This configuration makes it challenging to integrate the lasers with other Si-based photonic components such as waveguides, splitters, (de)multiplexers, and modulators that are exclusively processed on silicon-on-insulators (SOIs). Additionally, the emission wavelength of these nanolasers is limited to the O band (<1360 nm) [17]. For compact and efficient interchip/intrachip data communications, expanding the lasing spectra from the 1.3 μm band to the 1.5 μm band is desirable for larger circuit bandwidth and functionality.

In this work, we demonstrate a room-temperature in-plane InP/InGaAs nanolaser array epitaxially grown on (001) SOI substrates emitting at the 1.5 μm band. Starting with InP/InGaAs nanoridges selectively grown inside nanoscale Si trenches on SOI, we achieve strong on-chip mode confinement by designing air-surrounded nanocavities supported by partially etched Si pedestals, and thus obtain room-temperature stimulated emission under optical excitation. More significantly, the lasing peak can be tuned to cover the E band, the S band, and the C band through selection of the nanocavity length defined by lithography. Compared with our previous transferred InP/InGaAs nanoridge lasers with random orientations [19], the monolithic integration of well-aligned telecom nanolasers on (001) SOI wafers using selective-area heteroepitaxy combined with traditional top-down processing offers an intriguing path towards compact on-chip III–V light sources for Si photonics.

Figure 1(a) schematically delineates the designed InP/InGaAs nanolaser array directly grown on (001) SOI. We adopted a conventional FP cavity with etched end facets to examine the feasibility of our design. The in-plane InP/InGaAs nanolasers are underpinned by Si pedestals with a triangular-shaped cross section, the size of which is carefully controlled to ensure a strong mode confinement inside the nanoridge as well as robust mechanical support for the top laser cavity. Note that the supporting Si pedestal with atomic sharp {111} surfaces also serves as a low-loss waveguide to couple light out from the above laser cavity, providing potential on-chip light manipulation. The fabrication process is briefly outlined in Fig. 1(b). Starting with InP/InGaAs nanoridges grown on SOI substrates, the oxide spacers were selectively etched away using a buffered oxide etch. Then, aiming at minimizing light loss into the Si device layer, the underneath Si was undercut to a triangular-shaped post using potassium-hydroxide-based selective wet etch. In the next step, an oxide layer with a thickness of 300 nm was deposited onto the sample using plasma-enhanced chemical vapor deposition (PECVD). This PECVD oxide provides a uniform coverage of the nanoridges and the Si pedestals, and serves as a protection mask during the subsequent etching process. Finally, the end facets of nanolaser cavities with different lengths were defined using focused ion beam milling (FIB), and the oxide mask was selectively removed using a buffered oxide etch afterwards. Note that the nanolaser array demonstrated here could also be easily fabricated using traditional photolithography and the dry-etching process with other dimensions and thus by no means compromises their cointegration with other Si-based optical elements.
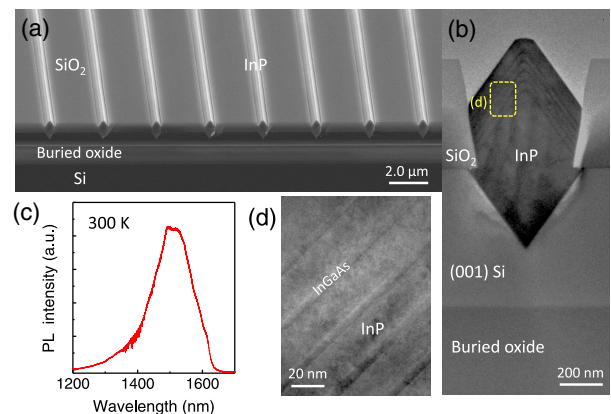
The InP/InGaAs nanoridges in this experiment were grown on (001) SOI substrates to ensure a strong on-chip mode confinement inside the as-grown nanoridges and compatibility with the current Si photonics platform. We started with commercial 100 mm (001) SOI wafers with a 2.0 ± 0.5 μm thick Si device layer, a 1.0 μm thick buried oxide layer, and a 500 μm thick Si handle layer. To reduce light leakage into the underlying Si device layer and confine light within the epitaxial III–V alloy, the SOI layer was thinned down to around 600 nm using cycled thermal oxidation and the subsequent buffered oxide etch process [20]. Then [110] oriented SiO_2 stripes, with a line pitch of 2.8 μm, a trench opening of 450 nm, and a trench length of 15 mm, were defined atop the Si device layer. The large separation of adjacent trenches ensures minimal light coupling between neighboring nanoridges to allow for probing
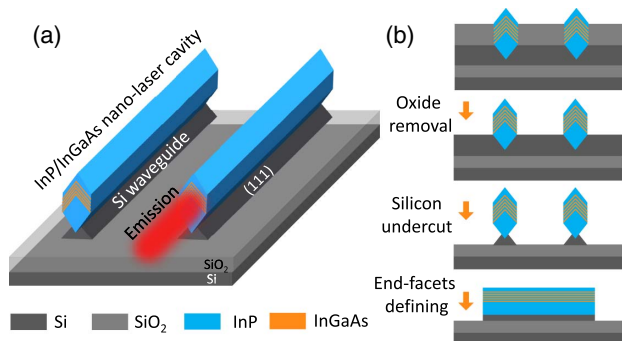
of the optical properties of individual nanocavities. After patterning, we grew InP/InGaAs nanoridges inside the nanoscale Si trenches using metal organic chemical vapor deposition. A detailed description and development of the heteroepitaxial process can be found in Refs. [21–23]. Figure 2(a) displays a 70° tilted-view scanning electron microscope (SEM) image of the as-grown sample, showing the equally spaced in-plane InP nanoridge array inside nanoscale Si trenches. Similar to nanoridges grown on Si substrates, structures grown on SOI also exhibit a faceted growth front with two convex {111} facets connected by a flat (001) facet [24]. The cross-sectional transmission electron microscope (TEM) photo of one nanoridge is presented in Fig. 2(b). With a width of 450 nm and a height of 1.0 μm, the nanoridges could efficiently guide optical modes at the telecom bands [25]. The large lattice mismatch between InP and Si is accommodated through the formation of a thin layer of high-density planar defects at the III–V/Si interface, rendering the upper InP main layer with high crystalline quality. We embedded five $In_{0.53}Ga_{0.47}As$ ridge quantum wells inside the InP nanoridge using a "cycled growth procedure" [19], as shown in Fig. 2(d). The atomically flat {111} facets developed during the selective-area growth process result in sharp interfaces between the ridge InGaAs and InP continuum, which in turn minimizes the interfacial nonradiative recombination and maximizes the light-emitting efficiency. At room temperature, the as-grown InP/InGaAs nanoridge array emits around 1500 nm and serves as the gain medium for wavelengths in the E, the S, and the C band [see Fig. 2(c)].

Figure 3(a) displays a tilted-view SEM image of the finalized InP/InGaAs nanolaser array on SOI. The end facets of the laser cavity were created by etching two parallel trenches with a length of 40 μm, a width of 15 μm, and a depth of 2.0 μm. Consequently, each nanolaser array consists of 15 equally distributed individual nanolasers. These nanolasers feature a highly ordered in-plane configuration with horizontal light emission. A close-up of the end facets of the InP/InGaAs nanocavities with the supporting Si pedestals and the buried oxide layer is presented in Fig. 3(b). The morphology of the end facets defined by FIB is pretty smooth, while the profile exhibits a slight incline towards the nanoridge tip. These nonvertical

Fig. 1. (a) Schematic of the designed InP/InGaAs nanolaser array grown on a SOI substrate. (b) Fabrication process of the InP/InGaAs nanolaser on SOI.

Fig. 2. (a) SEM image of the InP/InGaAs nanoridge array on (001) SOI. (b) TEM image of one nanoridge, showing inserted InGaAs ridge QWs and buried oxide layer. (c) Room-temperature photoluminescence spectra of the as-grown nanoridges. (d) Close-up of one side of the InGaAs ridge QWs.
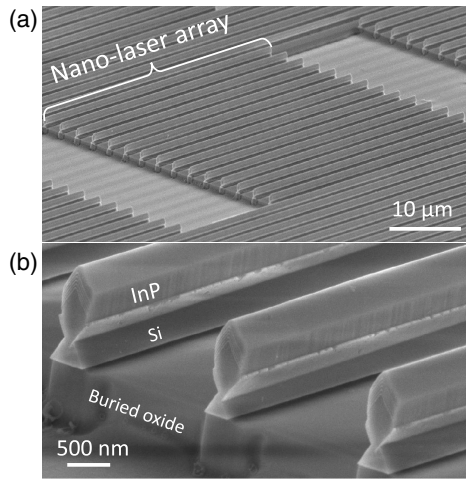
Fig. 3. (a) Tilted-view SEM image of the InP/InGaAs nanolaser array on (001) SOI. (b) Zoomed-in SEM image of the end facets of the nanolaser array.

Fig. 4. (a) Room-temperature emission spectra around threshold. Inset shows the emission spectra plotted in a logarithmic scale. (b) The evolution of the peak intensity and the linewidth as the excitation level increases. Inset presents the progression of peak position as a function of pumping levels.

profiles could in turn result in nonparallel end facets. However, the influence on the overall round trip loss should be inconsequential since optical feedback of the end facets comes from scattering instead of direct reflection because of the subwavelength dimension [26]. The size of the supporting Si pedestals also exhibits a variation, which could influence the mode distribution inside the nanocavity and accordingly affect the propagation loss and the modal gain. The fluctuation of the pedestal size results from the thickness variation of the initial SOI wafers, and a more uniform nanolaser array can be readily achieved using SOI substrates with better uniformity.

The on-chip nanolasers were characterized at room temperature using a home-built microphotoluminescence system, and laser oscillation was achieved under optical pumping by a mode-locked Ti/Sapphire laser (750 nm, 100 fs pulses, and a repetition rate of 76 MHz). The excitation laser beam was focused into a line-shaped spot by a cylindrical lens to cover the entire nanocavity. Figure 4(a) provides the emission spectra of one nanolaser with a length of 60 μm measured under different pumping fluences. At low pumping levels, the probed nanolaser features a broad spontaneous emission and well-spaced FP resonance peaks. As the pumping level increases, the peak at 1518 nm amplifies, protrudes from the background emission, and finally lases. The lasing behavior is further attested by the clamping of spontaneous emission around threshold, as shown by the emission spectra plotted in a logarithmic scale [see the inset of Fig. 4(a)]. Single-mode lasing is achieved, albeit the adoption of a simple FP cavity. Figure 4(b) displays the evolution of the peak intensity and the linewidth at 1518 nm as a function of the excitation levels. A clear S shape is detected from the L–L curve, and a lasing threshold around 40 μJ/cm² is extracted. This value is about double of that of the transferred nanolasers (smaller than 20 μJ/cm²) [19]. We attribute the somewhat larger lasing thresholds of nanolasers on SOI to the supporting Si pedestals, which lead to a reduced modal gain. Far above threshold, the intensity of the single-lasing mode at 1518 nm is orders of magnitudes higher than the clamped background emission, and a few weak side modes start to appear at the blue side. The linewidth of the lasing peak narrows from 1.2 nm to 0.8 nm around threshold, and then
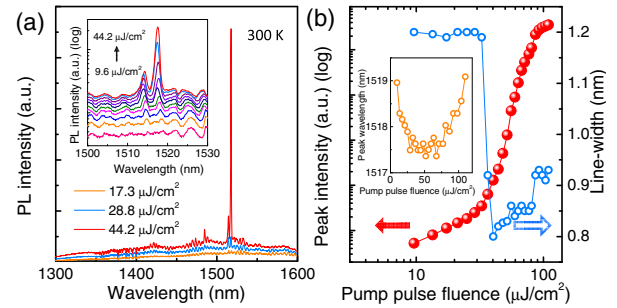
gradually augments to 0.9 nm as the excitation levels continue to increase. The subsequent broadening of the linewidth above threshold could be ascribed to wavelength chirp, where the fluctuation of carrier density induces the variation of refractive index [10,13,16]. The inset of Fig. 4(b) summarizes the progression of the peak position as the pumping level strengthens. The lasing mode initially blueshifts below threshold, then saturates around 1517.5 nm around threshold, and finally redshifts above threshold. The variation of the peak position is directly modulated by the alteration of refractive index. Three different mechanisms, namely band-filling effects, band gap shrinkage, and free-carrier absorption, contribute to carrier-induced change of the refractive index. For InP-based materials and a mode wavelength of 1.5 μm, the combination effect results in a reduced refractive index [27], which consequently causes the initial blueshift of the lasing peak. As the excitation level escalates and the nanolaser heats up, another effect called "thermal-induced change of refractive index" comes into play and leads to an increased refractive index [28]. The synergized effect of carrier-induced and thermal-induced changes of the refractive index brings on the saturation and following redshift of the lasing peak.

We also observed room-temperature lasing behavior from nanolasers with different cavity lengths. Figure 5(a) displays the measured photoluminescence spectra of one nanolaser with a length of 40 μm. Below threshold, we detect a broad spontaneous emission centered around 1.5 μm, modulated by evenly spaced FP longitudinal modes. The mode spacing around 1.5 μm is extracted as 5.7 nm corresponding to a group refractive index of 4.9. Above threshold, single-mode lasing is obtained at 1420 nm. The measured emission spectra of one nanolaser with a length of 50 μm is presented in Fig. 5(b). As expected, the spacing between adjacent longitudinal modes reduces to 4.5 nm. Interestingly, the lasing peak also redshifts to 1509 nm. Figure 5(c) summarizes the relationship of the lasing mode and the nanolaser length. Similar to the phenomenon observed from transferred nanolasers [19], the lasing wavelength of nanolasers grown on SOI exhibits a strong dependence on the length of the nanocavity, with a longer nanocavity corresponding to a larger emission wavelength. The correlation between the lasing mode and the cavity length might stem from the wavelength-dependent modal gain and propagation/end facet loss. A longer mode wavelength features a larger round trip loss and a smaller modal gain, and thereby necessitates
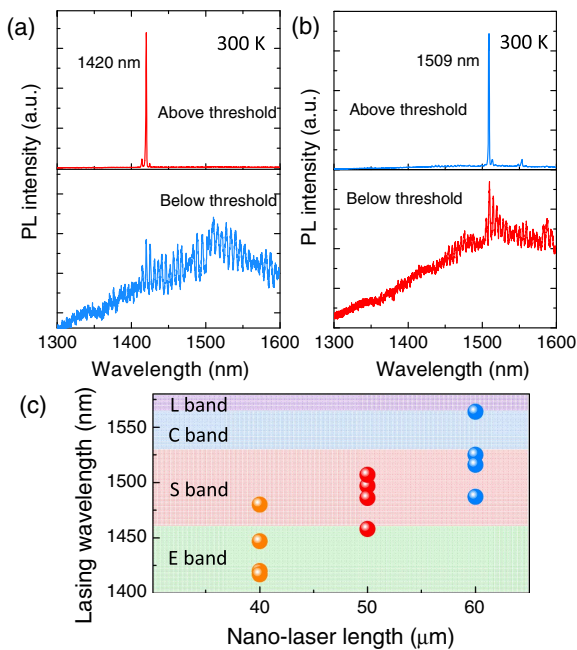
Fig. 5. (a) PL spectra of one nanolaser with a length of 40 μm measured below and above threshold. (b) PL spectra of one nanolaser with a length of 50 μm measured below and above threshold. (c) The relationship of the lasing peak and the length of the nanocavity.

a larger volume of active material to reach threshold. We will fabricate more nanolasers with a wider length variation to investigate the detailed mechanism.

In conclusion, we have demonstrated room-temperature InP/InGaAs nanolaser arrays monolithically integrated on (001) SOI substrate emitting at the telecom bands. Room-temperature laser oscillation corroborates the excellent optical quality of III–V nanoridges directly grown on Si, and affirms the validity of our proposed laser design. Incorporating an in-plane nanolaser array with Si-transparent light emission onto CMOS-compatible (001) SOI substrates suggests the feasibility of on-chip consolidation between compact III–V light sources and mature Si photonic components. Future work includes operating the nanolasers under continuous-wave excitation via advanced cavity designs, and realization of electrically driven telecom InP/InGaAs nanolaser arrays on (001) SOI.

REFERENCES

1. D. Thomson, A. Zilkie, J. E. Bowers, T. Komljenovic, G. T. Reed, L. Vivien, and D. Marris-Morini, J. Opt. **18**, 073003 (2016).
2. D. Liang and J. E. Bowers, Nat. Photonics **4**, 511 (2010).
3. Z. Zhou, B. Yin, and J. Michel, Light Sci. Appl. **4**, e358 (2015).
4. Z. Wang, A. Abbasi, U. Dave, A. De Groote, S. Kumari, B. Kunert, C. Merckling, M. Pantouvaki, Y. Shi, B. Tian, K. Van Gasse, J. Verbist, R. Wang, W. Xie, J. Zhang, Y. Zhu, J. Bauwelinck, X. Yin, Z. Hens, J. Van Campenhout, B. Kuyken, R. Baets, G. Morthier, D. Van Thourhout, and G. Roelkens, Laser Photon. Rev. **11**, 1700063 (2017).
5. S. Chen, W. Li, J. Wu, Q. Jiang, M. Tang, S. Shutts, S. N. Elliott, A. Sobiesierski, A. J. Seeds, I. Ross, P. M. Smowton, and H. Liu, Nat. Photonics **10**, 307 (2016).
6. A. Y. Liu, C. Zhang, J. Norman, A. Snyder, D. Lubyshev, J. M. Fastenau, A. W. K. Liu, A. C. Gossard, and J. E. Bowers, Appl. Phys. Lett. **104**, 041104 (2014).
7. Y. Wan, J. Norman, Q. Li, M. J. Kennedy, D. Liang, C. Zhang, D. Huang, Z. Zhang, A. Y. Liu, A. Torres, D. Jung, A. C. Gossard, E. L. Hu, K. M. Lau, and J. E. Bowers, Optica **4**, 940 (2017).
8. R. Yan, D. Gargas, and P. Yang, Nat. Photonics **3**, 569 (2009).
9. D. Saxena, S. Mokkapati, P. Parkinson, N. Jiang, Q. Gao, H. H. Tan, and C. Jagadish, Nat. Photonics **7**, 963 (2013).
10. J. Tatebayashi, S. Kako, J. Ho, Y. Ota, S. Iwamoto, and Y. Arakawa, Nat. Photonics **9**, 501 (2015).
11. R. Chen, T.-T. D. Tran, K. W. Ng, W. S. Ko, L. C. Chuang, F. G. Sedgwick, and C. Chang-Hasnain, Nat. Photonics **5**, 170 (2011).
12. B. Mayer, L. Janker, B. Loitsch, J. Treu, T. Kostenbader, S. Lichtmannecker, T. Reichert, S. Morkötter, M. Kaniber, G. Abstreiter, C. Gies, G. Koblmüller, and J. J. Finley, Nano Lett. **16**, 152 (2015).
13. H. Kim, W.-J. Lee, A. C. Farrell, J. S. D. Morales, P. Senanayake, S. V. Prikhodko, T. J. Ochalski, and D. L. Huffaker, Nano Lett. **17**, 3465 (2017).
14. F. Lu, I. Bhattacharya, H. Sun, T.-T. D. Tran, K. W. Ng, G. N. Malheiros-Silveira, and C. Chang-Hasnain, Optica **4**, 717 (2017).
15. H. Kim, W.-J. Lee, A. C. Farrell, A. Balgarkashi, and D. L. Huffaker, Nano Lett. **17**, 5244 (2017).
16. Z. Wang, B. Tian, M. Pantouvaki, W. Guo, P. Absil, J. Van Campenhout, C. Merckling, and D. Van Thourhout, Nat. Photonics **9**, 837 (2015).
17. B. Tian, Z. Wang, M. Pantouvaki, P. Absil, J. Van Campenhout, C. Merckling, and D. Van Thourhout, Nano Lett. **17**, 559 (2016).
18. Y. Shi, Z. Wang, J. Van Campenhout, M. Pantouvaki, W. Guo, B. Kunert, and D. Van Thourhout, Optica **4**, 1468 (2017).
19. Y. Han, W. K. Ng, C. Ma, Q. Li, S. Zhu, C. C. S. Chan, K. W. Ng, S. Lennon, R. A. Taylor, K. S. Wong, and K. M. Lau, Optica **5**, 918 (2018).
20. H. Kim, A. C. Farrell, P. Senanayake, W.-J. Lee, and D. L. Huffaker, Nano Lett. **16**, 1833 (2016).
21. Y. Han, Q. Li, S.-P. Chang, W.-D. Hsu, and K. M. Lau, Appl. Phys. Lett. **108**, 242105 (2016).
22. Y. Han, Q. Li, and K. M. Lau, J. Appl. Phys. **120**, 245701 (2016).
23. Y. Han, Q. Li, K. W. Ng, S. Zhu, and K. M. Lau, Nanotechnology **29**, 225601 (2018).
24. G. Biasiol, A. Gustafsson, K. Leifer, and E. Kapon, Phys. Rev. B **65**, 205306 (2002).
25. Y. Han, Q. Li, S. Zhu, K. W. Ng, and K. M. Lau, Appl. Phys. Lett. **111**, 212101 (2017).
26. M. A. Zimmler, F. Capasso, S. Müller, and C. Ronning, Semicond. Sci. Technol. **25**, 024001 (2010).
27. B. R. Bennett, R. A. Soref, and J. A. Del Alamo, IEEE J. Quantum Electron. **26**, 113 (1990).
28. J. A. McCaulley, V. M. Donnelly, M. Vernon, and I. Taha, Phys. Rev. B **49**, 7408 (1994).